

Hornnes, Vegard; Salganik, Evgenii; Høyland, Knut Vilhelm (2025)

Relationship of physical and mechanical properties of sea ice during the freeze-up season in Nansen Basin. *Cold Regions Science and Technology*, 229, 104353.

<https://doi.org/10.1016/j.coldregions.2024.104353>

The attached document is the accepted manuscript version of the publication above and is published in accordance with §38(4) UrhG twelve months after the original publication.

Institutional Repository:

<https://epic.awi.de/>

HELMHOLTZ



Relationship of physical and mechanical properties of sea ice during the freeze-up season in Nansen Basin

Vegard Hornnes^{a,*}, Evgenii Salganik^b, Knut Vilhelm Høyland^{a,c}

^a Norwegian University of Science and Technology, Department of Civil and Environmental Engineering, Høgskoleringen 7A, 7491 Trondheim, Norway

^b Norwegian Polar Institute, Fram Centre, Hjalmar Johansens gate 14, 9296 Tromsø, Norway

^c The University Centre in Svalbard (UNIS), 9171 Longyearbyen, Norway

ARTICLE INFO

Keywords:

Field measurements
Sea-ice properties
Porosity
Borehole jack
Strength
Variability

ABSTRACT

Sea-ice properties, such as porosity and strength, can have significant spatial variability at small scales. Quantifying this variability may give better estimates of the ice properties and their interrelation. Additionally, correlating in situ ice strength measurements and ice properties, including porosity, may improve understanding of the factors influencing ice strength. This paper presents measurements of sea-ice properties and strength on first- and second-year sea ice during the GoNorth expedition to the Arctic Ocean in October 2022. In situ borehole indentation measurements were co-located with measurements of physical properties, and the meter-scale variability of the physical properties and strength was investigated. Bulk density values found from hydrostatic weighing were $911 \pm 5 \text{ kg m}^{-3}$ for first-year and $904 \pm 5 \text{ kg m}^{-3}$ for second-year ice, with significantly less uncertainty than density values from the mass/volume method or from freeboard/draft measurements. The second-year ice was relatively saline, with a mean bulk salinity of 3.1 ± 0.5 , and the ice was desalinated in the upper and lower 0.2 m. The bulk gas fraction in the second-year ice was $2.5 \pm 0.5 \%$, similar to the first-year ice gas fraction of $2.8 \pm 0.5 \%$. Gas fractions up to 6.5 % were observed in the second-year ice without any obvious correlation with the brine fraction. The second-year ice had larger spatial variability in thickness, porosity, grain structure, and ice strength compared to the first-year ice. Variability in bulk density and gas fraction were similar for first- and second-year ice, as the larger variability was mostly seen below the upper 0.4 m of the second-year ice. The borehole strength was $26.0 \pm 4.4 \text{ MPa}$ for first-year and $41.0 \pm 12.1 \text{ MPa}$ for second-year ice. There were indications that the total microporosity at indentation depth was related to in situ borehole strength ($R^2 = 0.82$), and that brine volume was the most influential parameter. The relative variability in the local microporosity in the second-year ice (0.43) was greater than the relative variability in borehole strength (0.27), while the opposite was true for the first-year ice (0.09 versus 0.17).

1. Introduction

The physical and mechanical properties of first- and second-year ice are important for both the interpretation of large-scale sea-ice observations and the accurate modelling of sea-ice thermodynamics and dynamics. Ice properties are also used to estimate the severity of any ice-structure interaction. Meanwhile, studies about such properties often focus on their seasonal evolution. Studying the spatial variability of sea-ice properties may improve confidence in our analysis of all year-round data.

1.1. Study area

The sea-ice cover in the area north of Svalbard is strongly affected by the presence of the West Spitsbergen Current (Fig. 1a), which turns eastward and splits into several sub-branches near the Yermak Plateau (Koenig et al., 2017; Lundesgaard et al., 2022). The branches crossing the Plateau converge to form the Fram Strait Branch of the Atlantic Water Boundary Current in the Arctic Ocean, which flows eastward along the continental slope of the Nansen Basin (Woodgate et al., 2001). The last 20 years were characterized by a dramatic decline and strong year-to-year variability in Barents Sea winter sea ice, with its variability suggested to be driven by both atmospheric (Liu et al., 2022) and

* Corresponding author.

E-mail addresses: vegard.hornnes@ntnu.no (V. Hornnes), evgenii.salganik@proton.me (E. Salganik), knut.hoyland@ntnu.no (K.V. Høyland).

oceanic (Årthun et al., 2019) processes. Peterson et al. (2017) showed a large spatial variability of ocean heat fluxes in the area north of Svalbard, with typical Arctic conditions in the Nansen basin and large ocean heat fluxes near the Yermak Plateau.

1.2. Spatial and temporal variability of physical properties

Sea-ice freeboard (height above the waterline) depends on snow, sea-ice densities, and thicknesses and plays an important role in aerial and satellite altimetry (Dawson et al., 2022). Inaccuracies in the assumed snow and sea-ice density can lead to substantial inaccuracies in the estimated ice thickness (Alexandrov et al., 2010). For example, typical ice density variations of 840–910 kg m⁻³ (Timco and Frederking, 1996) can lead to variations in sea-ice thickness estimates of 0.4–0.8 m, given typical ice freeboard values (Kern et al., 2015). The most commonly used sea-ice density datasets used for remote sensing purposes have several limitations, such as being restricted in time and not including the melt season, where one might expect a significant density change due to flushing and gas fluxes. Thus, there is a need for accurate, local sea-ice density data during more parts of the year. Meanwhile, Kern et al. (2015) noted that sea-ice density is as important as snow depth for using radar altimetry for sea-ice thickness retrieval, while Landy et al. (2020) estimated the potential systematic bias in CryoSat-2-derived sea ice thickness introduced by sea-ice density as 0.31–0.37 m.

1.2.1. Sea-ice density

The density of sea ice depends on the volumetric fractions of gas and liquid brine. These volumetric fractions are usually estimated from direct measurements of sea-ice salinity, density, and temperature (Cox and Weeks, 1983; Leppäranta and Manninen, 1988). During the ice growth phase, the bulk brine fraction is usually below 5 % (Griewank and Notz, 2013) and the gas volume fraction below the waterline is usually less than 2 % (Crabeck et al., 2016), which explains the relatively small variability of winter sea-ice density. The most common methods for sea-ice density measurements are the mass/volume method with a 3–8 % error (Hutchings et al., 2015) and hydrostatic weighing with a 0.1–1.3 % error (Nakawo, 1983). Higher errors for the mass/volume method are related to the large uncertainties of sample volume estimates based on their assumed geometry and linear dimensions, which is not required for hydrostatic weighing (Pustogvar and Kulyakhtin, 2016). Timco and Frederking (1996) estimated the usual range of first-year ice (FYI) bulk density of 840–910 kg m⁻³ with 900–940 kg m⁻³ for the density below the waterline. Alexandrov et al.

(2010) used measurements of ice freeboard and thickness to estimate FYI density of 917 ± 36 kg m⁻³ using the data from the Eurasian Russian Arctic collected in February–May of 1980–1988. They also estimated bulk MYI density to be 882 ± 23 kg m⁻³, though this estimate was not based on direct measurements. Jutila et al. (2022) used a combination of airborne freeboard and ice thickness measurements collected in the western Arctic Ocean in April 2017–2019 to estimate first-year ice (FYI), second-year ice (SYI), and multiyear ice (MYI) density of 925 ± 18 kg m⁻³, 899 ± 17 kg m⁻³, and 902 ± 19 kg m⁻³, respectively. Note that their measured SYI was 3–5 times thicker than the adjacent FYI, which may have contributed to the density difference. Fons et al. (2023) used Antarctic sea-ice density of 875 (summer), 900 (autumn), 920 (winter), and 915 (spring) kg m⁻³ based on the field measurements from Worby et al. (2008). For Arctic, Salganik et al. (2023c) showed FYI gas volume increase from 2 % to 6 % and the absence of such strong increase for second-year ice (SYI) during July using a hydrostatic method, while Wang et al. (2020) estimated an FYI average gas fraction of 15 % in August using the mass/volume method. During autumn, FYI gas fraction from hydrostatic measurements during MOSAiC decreased within two weeks from 4 % in early November to 2 % in late November, with SYI gas fraction staying close to 1 % (Salganik et al., 2023c). Rare autumn FYI density was reported by Sinha (1984) and Forsström et al. (2011), with values of 902 ± 7 kg m⁻³ in mid-September and 907 ± 2 kg m⁻³ in mid-October, showed low and increasing FYI density at the beginning of the freezing period. Crabeck et al. (2016) used computed tomography to show that processes of salt redistribution do not control the distribution of gas in sea ice. Usually, gas uptake in sea ice occurs by freeze-up events of supersaturated seawater (Crabeck et al., 2014). Moreau et al. (2014) showed that the source of abiotic gases is associated with the nucleation of gas bubbles due to the supersaturation of dissolved gases in brine inclusions and measured argon accumulation in the bottom half of sea ice during its growth.

Most estimates show that FYI bulk density outside of melt season is similar to pure ice density of 917 kg m⁻³, while SYI is lighter than pure ice. This indicates a larger or equal effect of the gas fraction on sea-ice density in comparison to brine volume. As brine volume directly depends on sea-ice temperature, mainly defined by air temperature, snow, and ice thickness; it is beneficial to separately analyse the spatial variability and seasonal evolution of the sea-ice gas fraction. While some models (Griewank and Notz, 2013) may accurately predict salinity evolution for FYI and SYI, such models do not exist for gas fraction (Crabeck et al., 2016). Meanwhile, Salganik et al. (2024) showed a strong seasonality of summer sea-ice density and gas volume based on

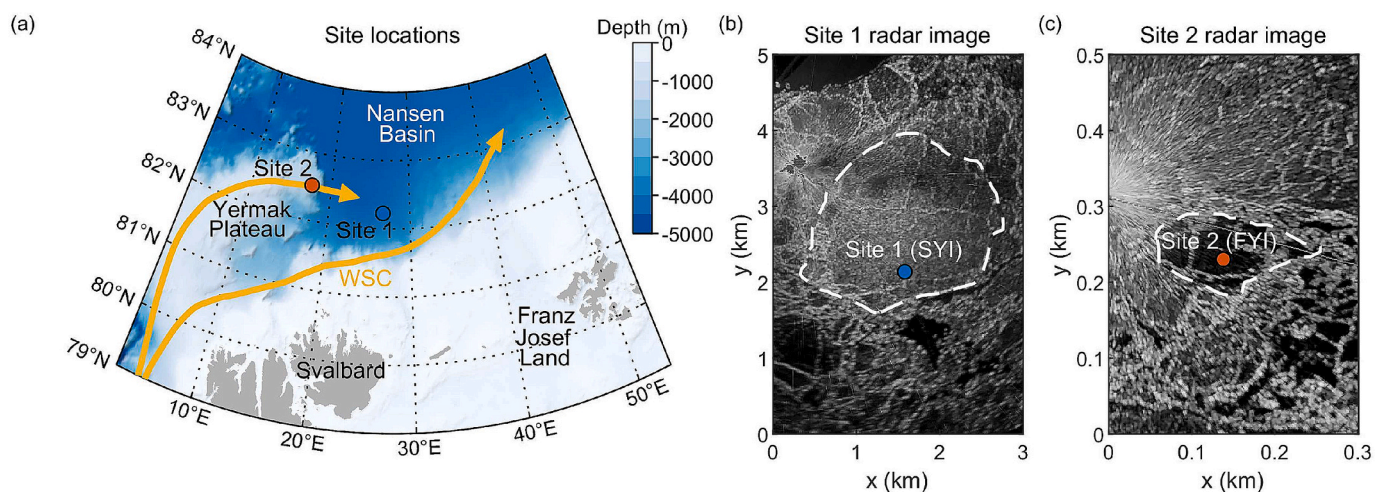


Fig. 1. Bathymetry in the study region, with the two ice stations and major geographic features labeled (a). Marine radar images showing the investigated ice floes (white dashed line) and ice stations (b,c). Displayed bathymetric data in (a) are from ETOPO2 (National Geophysical Data Center, 2006). Orange arrows in (a) indicate the West Spitsbergen Current (WSC) and its branches entering the Nansen Basin following Lundesgaard et al. (2022).

weighing and freeboard/draft measurements on various scales.

1.2.2. Sea-ice salinity

The accuracy of sea-ice salinity measurements using the mass/volume method may strongly affect density measurements through brine losses, while for a hydrostatic method, the error of density measurements is limited by 2 % (Pustogvar and Kulyakhtin, 2016). Notz and Worster (2008) identified the main desalination processes as gravity drainage and flushing of surface meltwater and melt ponds. Gravity drainage has been successfully modeled using a 1-D sea-ice model and can be triggered both by atmospheric heat and bottom melt from oceanic heat (Griewank and Notz, 2013), while Vancoppenolle et al. (2007) formulated the first parametrization of the ice flushing mechanism. Meltwater flushing results in a bulk salinity of 2–3 for multiyear ice (Untersteiner, 1968). Eicken (1994) observed significant differences in salinity profiles of level ice with (0.4–0.7) and without (3.1) an under-ice meltwater layer, indicating desalination by meltwater flushing (ice with and without meltwater layer was 1.6 m and 3.2 m thick, respectively). Salganik et al. (2023b) observed FYI bulk salinity reduction from 5.2 to 1.1 during May and July 2022 during the MOSAiC expedition in the Fram Strait with the presence of under-ice meltwater layers. The measurements from Wang et al. (2020) for the Pacific Sector of the Arctic Ocean in August of 2008–2018 with an average salinity of 1.9 for FYI and 1.3 for multi-year ice (MYI) were approximately twice as large as for MOSAiC. Vancoppenolle et al. (2009) showed that both observations and modelling give FYI salinity of 1–2 from June to September, while simulations also give higher FYI salinity of 3–4 in September for areas North of Franz Josef Land.

1.3. Mechanical properties

The mechanical properties of ice are important not only for ships and structures in ice-infested waters but also for sea-ice deformation and ridging. So far, the mechanical characteristics used in sea-ice models are not based on quantifiable ice properties. Sea ice has most of the complicating elements of material mechanics; it is elastic, viscous, and brittle, and this deterministic mechanical behaviour is only partly understood. However, it is clear that the ice porosity (gas and brine fractions) has an influence on its behaviour (Timco and Weeks, 2010).

Much of the previous research into the link between certain sea-ice physical properties and different forms of ice strength has focused on correlating ice strength with temperature and salinity, which would allow estimations of brine porosity through the empirical relations from Frankenstein and Garner (1967). However, fewer studies have included density measurements, which are more demanding to carry out but would enable a more accurate calculation of the total porosity (Cox and Weeks, 1983; Leppäranta and Manninen, 1988). When density measurements have been conducted, they have often been based on mass/volume calculations instead of hydrostatic measurements, with the associated increase in experimental error. For example, summer (early August) sea-ice microporosity along with flexural and uniaxial compressive strength was studied by Wang et al. (2023) with a significant correlation between strength and microporosity. In their study, the density for 1.3–1.6 m thick FYI was calculated using the mass/volume method, which led to a potentially overestimated gas fraction of 1.8–36.9 % for individual ice samples with a 0.07 m width, which is supported by low brine fractions of only 0–3.8 %.

Uniaxial compression tests are the most common field tests of ice strength, and Moslet (2007) summarized several previous works where the uniaxial compressive strength and physical properties of FYI were measured. They also analysed measurements of both physical properties and uniaxial compression, and found the maximum strength (in MPa) for horizontal ice cores could be estimated using the total porosity v_T (as a fraction of the total volume) through the equation $8(1.4v_T - 2(1.4v_T)^{0.5} + 1)$. Note that the author based their density

measurements on mass/volume calculations. Timco and Frederking (1990) proposed a proportionality of $v_T^{0.5}$ between total porosity and uniaxial strength for FYI, but they used an estimation of the bulk density of sea ice for their predictions of compressive strength, with the assumption of constant density throughout the autumn and winter months. Despite this, the authors do point out that the density can have a significant influence on the estimated ice strength, highlighting the need for accurate density measurements. Kovacs (1997) estimated full-scale physical properties and strength and estimated that the full-thickness horizontal compressive strength scaled with the inverse of the bulk porosity.

A different method to characterise the ice strength is through the use of a borehole jack. Borehole jack measurements are based on drilling a borehole and indenting horizontally into the borehole wall, measuring the indentation force. The borehole jack is an established measurement technique and is referred to in the ISO standard for Arctic offshore structures as a way to scale ice strength between different regions (ISO 19906, 2019). Borehole jack measurements should have inherent advantages for testing the correlation between the physical properties of the ice and its strength, as the strength is measured in situ with minimal risk of brine drainage and temperature changes (Sinha, 2011). In particular, brine drainage can be a challenge for uniaxial compression tests and can affect the estimations of brine volume (Moslet, 2007).

Previous borehole jack investigations have been carried out in a wide range of sea ice of different ages, as summarized by Johnston (2017). To understand the borehole strength and its interrelation to the physical properties of the ice, previous investigations have primarily focused on the significance of temperature and salinity. Johnston (2006, 2014) used temperature and salinity to estimate the brine volume from the empirical relations proposed by Frankenstein and Garner (1967), while the gas volume fraction was not estimated due to a lack of sea-ice density measurements. They found a decreasing strength with increasing brine volume as the ice decayed and temperature increased. Johnston (2014) suggested an exponential model for their borehole strength in multi-year ice, using the square root of the brine volume, but with poor results. They concluded that, especially for multi-year ice, it is preferable to include data on air porosity, but they also suggest that the bulk density around the borehole may be relevant. Johnston (2006) points out that it is difficult to separately distinguish the effects that increasing temperature and increasing porosity have on strength because these are intrinsically linked for sea ice. But as Johnston points out, increasing brine volume due to increasing temperature is only part of the equation, and an appreciable portion of the porosity can consist of entrapped gas. However, to our knowledge, there are no published works where the relation between the total ice microporosity, including gas volume, and in situ indentation strength is investigated.

1.3.1. Spatial variability of strength

Sea ice has large temporal and spatial variability on all practical scales. The variability will manifest itself in both the sea-ice physical and mechanical properties. For the mechanical properties, characterizing the spatial variability can help close the gap between mechanical tests of sea ice and parameterization in sea-ice models. Additionally, an improved understanding of spatial variability is of interest for models simulating stochastic interactions between sea ice and structures (Hendrikse and Nord, 2019).

There is a good correlation between the physical parameters of sea ice and its thickness (Kovacs et al., 1996). Second-year ice (SYI) has higher spatial variability than first-year ice, both when it comes to thickness and physical properties, because of the summer processes. Most of the spatial variability of SYI comes from uneven surface melt due to ice-albedo feedback and uneven bottom melt (Webster et al., 2022). Thin and ponded ice is stronger subjected to desalination via flushing (Eicken, 1994) and to warming by under-ice meltwater layers (Salganik et al., 2023b). Due to the greater spatial variability in the SYI, it is

expected that the ice also exhibits greater variability in mechanical properties. However, there is a clear lack of studies investigating the spatial variability of density, which is needed to find the variability of total porosity across different types of ice. Studies investigating the spatial variability of strength have typically focused on uniaxial compressive strength. For example, [Strub-Klein and Høyland \(2012\)](#) found that the strength variability increased with increasing brine fraction up to 0.05, and younger ice with smaller brine channels had more consistent strength.

Compared to uniaxial compression, borehole strength measurements might give a more accurate understanding of the undisturbed spatial variability in sea-ice strength, due to the reduced risk of disturbing the ice. To the authors' knowledge, the spatial variability of borehole strength and possible connections to the spatial variability of the physical properties of the ice has not previously been investigated in published literature. The spatial variability in borehole strength may not be the same as uniaxial compressive strength, as a larger volume of ice is tested with a different geometry. Additionally, the influence of other extrinsic factors (e.g., sample preparation, crack nucleation points) will be different for uniaxial compression than indentation. Due to the spatial variability in ice being anisotropic, where much of the variability may originate from brine drainage channels, a different geometry may result in a different spatial variability.

The purpose of this paper is to present the physical properties of two types of Arctic sea ice during October, including ice temperature, salinity, density, and porosity, and examine their possible connection with in situ ice indentation strength.

2. Materials and methods

Measurements of ice and snow thickness, freeboard, and a range of ice properties were made during leg 1 of the 2022 GoNorth scientific expedition (cruise number 2022713) to the Arctic Ocean aboard the icebreaker RV *Kronprins Haakon* from 14 October to 3 November 2022. Measurements were made at two stations, shown in [Fig. 1a](#). The first station, investigated on 24 October, was located at 82°13.56' N, 26°41.43' E on a second-year ice (SYI) or multiyear ice floe measuring approximately 2.4 km by 2.4 km, and with a thickness of 1.09 ± 0.1 m. The geometries of the investigated ice floes are shown in [Fig. 1b,c](#). The SYI floe had substantial surface roughness typical for old and deformed ice. The second station, investigated on 30 October, was at 82°31.05' N, 17°30.04' E on a first-year ice (FYI) floe measuring approximately 0.2 km by 0.1 km, with ice thickness of 0.31 ± 0.01 m. Snow depths were 8 ± 4 cm and 3 ± 1 cm for the study areas of the SYI and FYI floes,

respectively. On 24 October, the average air temperature was -19.6 °C, water temperature was -1.7 °C, and the wind speed was 8 m s^{-1} , while on 30 October the average air temperature was -8.0 °C, water temperature was -1.6 °C, and the wind speed was 12 m s^{-1} .

Eleven and 17 ice cores were collected at the first and second stations, respectively, where 21 cores were used for the investigation of physical properties and microstructure. Grids with 5 m spatial resolution were defined on both the SYI and FYI, where ice cores were sampled and mechanical measurements were carried out at each grid point. To examine the origin of the ice observed at the coring sites, we computed backwards particle trajectories using the daily sea-ice drift vectors from Polar Pathfinder with 25 km resolution ([Tschudi et al., 2019](#)) following the methodology described in ([Sumata et al., 2023](#)). Based on ice thickness estimates from CryoSat-2, the studied SYI site was characterized by thick ice prior to the melt season. Mean ice thickness in March 2022 was 3.3–3.4 m for back-tracked SYI site (spring radar altimetry estimates often have nearly 100 % overestimation of ice thickness due to wet snow), while by late July it linearly decreased to 1.6 m ([Landy et al., 2022](#)), shown in [Fig. 2](#). The ice melt of 1.7–1.8 m by late July indicates large ocean heat fluxes (OHF) in the investigated areas, as typical Arctic conditions correspond to approximately 1.0 m of total ice melt after the melt season ([Perovich et al., 2011](#)). In late July, site 1 (SYI) included 70 % of multiyear ice, while site 2 (FYI) consisted of 90 % multiyear ice fraction. The merged CryoSat-2 and SMOS-derived thickness estimate is 0.5–0.8 m for SYI site and 1.6 m for FYI site on 24–30 October ([Ricker et al., 2017](#)). It also showed that ice thickness for back-tracked SYI site increased from 0.9 m in October 2021 to 2.4 m in March 2022 and decreased to 0.7 m in October 2022, showing similar large ice melt of 1.7 m. On October 24, the ice edge north of Svalbard was close to the monthly median edge, while on 30 October, there was a substantial edge retreat in the northeastern part of Svalbard.

2.1. Measurements of physical properties

For the ice at each station, we carried out salinity, temperature, and density measurements of the retrieved ice cores. The ice cores were collected within 2 m with measurements of ice thickness, snow depth, freeboard, and ice strength, in grids of 3 by 3 for the first station and 3 by 4 for the second, with 5 m horizontal resolution. Ice cores with 72.5 mm diameter were extracted via a Kovacs Mark III Core Barrel. After extraction, the lengths of the cores were measured and promptly used for either temperature measurements, or packed in plastic bags and stored on sleds. After the end of the work, these cores were then transported back to the ship and into a freezer room holding -20 °C. For ice

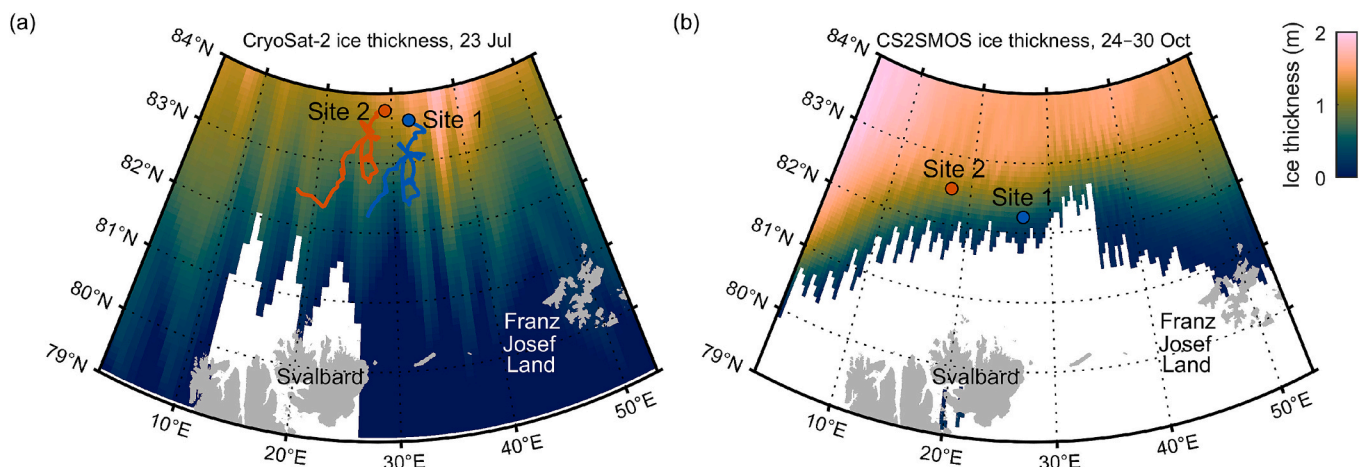


Fig. 2. Sea-ice thickness from CryoSat-2, [Landy et al. \(2022\)](#) (a) and from CryoSat-2 and SMOS, [Ricker et al. \(2017\)](#) (b). The location of coring sites on 23 July (a) was estimated using back-trajectories from the daily sea-ice drift vectors from Polar Pathfinder ([Tschudi et al., 2020](#)). Contour plot colours follow recommendations of scientifically derived colour maps ([Cramer et al., 2020](#)).

temperature measurements, one temperature profile was made per measurement station, where 3 mm wide holes were drilled into an extracted core with 5 cm vertical resolution. The temperature was measured by inserting the probe of an Ebro TFX410 thermometer into the holes and allowing the temperature to stabilize. Density measurements were carried out by sectioning each core in 4 cm to 6 cm long pieces in a cold lab aboard the ship following the days after extraction, followed by hydrostatic density measurements (Pustogvar and Kulyakhtin, 2016). Each piece was allowed to melt in separate, closed containers, and salinity was measured with calibrated conductivity meters (YSI MT30 and Mettler Toledo SevenGo S3), the conductivity is converted to salinity and reported on the Practical Salinity Scale 1978, PSS-78, which is dimensionless. The relative brine and gas volume of each sectioned piece was calculated following the method by Cox and Weeks (1983) and Leppäranta and Manninen (1988), where the volumes were back-calculated to in situ values using the ice temperature profile measured in the field. For the calculation, this work assumes that gas and brine pockets are connected (Crabeck et al., 2016). One core per measurement station was sectioned and used only for salinity measurements. Two ice cores per measurement station were transported in cooling boxes holding -18°C to Trondheim, Norway, for microstructure characterization. Thin sections of the cores were prepared using a modified double-microtoming technique (Sinha, 1977; Shokr and Sinha, 2015), and the microstructure was examined using polarized light in a Rigsby stage (Langway, 1958).

2.2. Mechanical measurements

The confined, in situ indentation strength of the ice was measured with the use of the NTNU mechanical borehole jack (BHJ), shown in Fig. 3. The system is described in detail by Kallelid et al. (2019). The BHJ is used to indent horizontally into a borehole wall after augering, to measure the resisting force from the ice. The BHJ has a cylindrical, smooth surfaced piston with 30 mm diameter, where the indenter surface is curved to approximately match the curvature of the augered borehole. The BHJ is driven by a Makita DDF481 electric drill, giving almost constant indentation speed. At each grid point, boreholes were made by a 77 mm wide auger and the BHJ was inserted. Water typically intruded into the borehole after augering, but indentation was carried out as soon as possible after augering to avoid any effects of temperature changes in the ice. The indentation was carried out into each borehole

at a rate of 0.5 mm s^{-1} to 1.1 mm s^{-1} as a mean over the entire indentation. Loads were recorded at 200 Hz frequency, and drill batteries were replaced after approx. 10 indentations to ensure a consistent indentation speed. The indentations were generally made in the middle of the ice sheet, meaning 0.5 m from the top of the ice for the SYI and 0.16 m for the FYI. Exceptions were made for the deformed areas at coordinates (5,15) and (10,15) on the SYI site, where the ice was not solid all the way through. At these coordinates, the indentation was made at 0.31 m and 0.27 m below the ice surface, respectively, in the middle of the hard top ice layer. As the BHJ uses a single indenter, two indentations were carried out per borehole in opposite directions (in positive and negative y-directions), and the mean of the peak pressures was taken. Twenty-four measurements in SYI and 18 measurements in FYI were made.

During borehole indentation, a large variety of failure responses may be observed. As summarized by Johnston (2017), the variety of behaviours during indentation makes it challenging to establish a universal definition of ice strength. A well-defined yield point is not always observed during the indentation, and when a peak is observed, there is a possibility that an even larger pressure peak could have occurred if the indentation had continued beyond the 30 mm maximum indentation. Existing borehole strength classification systems are based on hydraulic jacks with variable indentation rates, and significant differences can be observed in the load response compared to the mechanical system used in this work. In this work, the highest (maximum) pressure recorded during indentation will be defined as the borehole strength to ensure consistency with previous work using a similar borehole jack system (Kallelid et al., 2019; Rødtang et al., 2023).

3. Results and discussion

3.1. Sea-ice density and salinity

The vertical profiles of salinity, along with the estimated brine and gas fractions for the FYI and SYI, are shown in Fig. 4. The SYI salinity and brine fraction profiles could roughly be divided into two groups, where one group was considerably less desalinated below approx. 0.2 m. In contrast, the FYI exhibited less variability, except for in the upper 0.05 m. The bulk physical properties, along with the estimated bulk brine and gas fraction of the FYI and SYI, are summarized in Table 1.

The variability of sea-ice density was mostly related to the variability

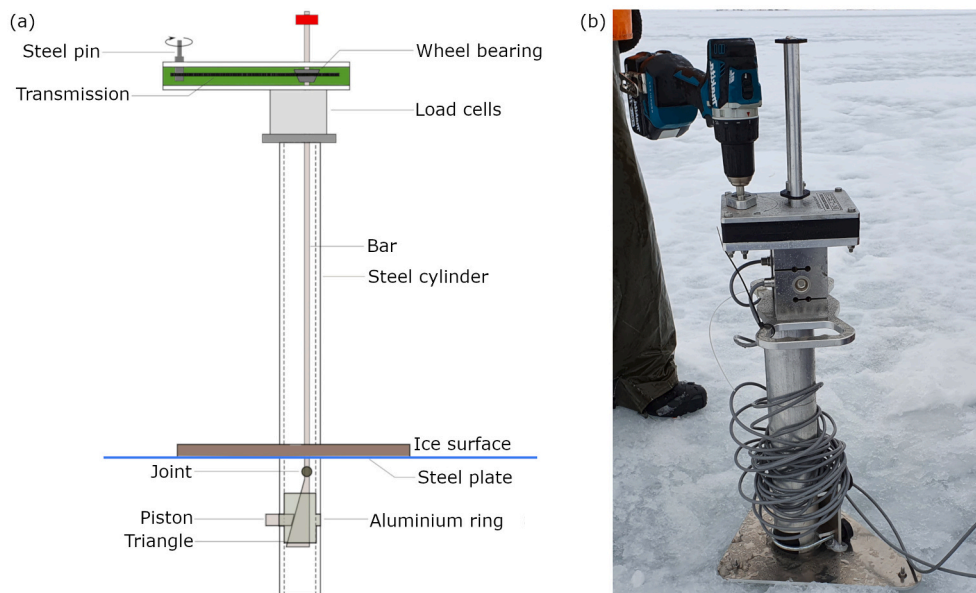


Fig. 3. Schematic of the NTNU BHJ (a), modified from Kallelid (2018), and a picture of the BHJ inserted into a borehole (b).

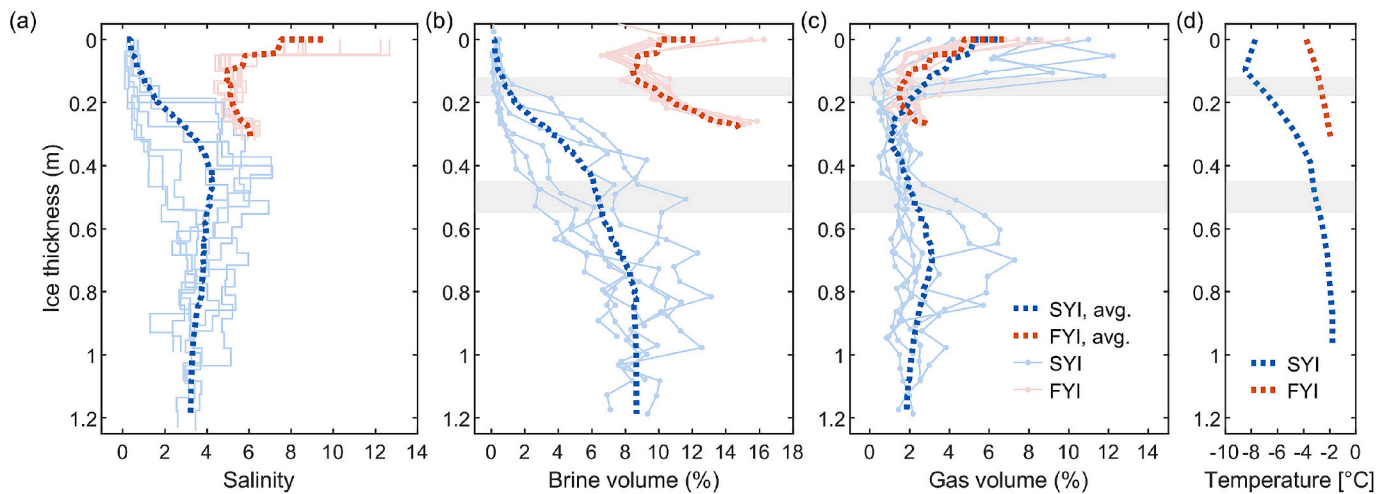


Fig. 4. Vertical profiles of salinity (a), brine volume fraction (b), gas volume fraction (c), and temperature (d) through the ice. All profiles are shown as light solid lines, with average profiles shown as dotted lines for each ice type. The depths of indentation are highlighted by two horizontal bands centered at -0.16 m for FYI and -0.50 m for SYI. The average profiles were obtained using a Savitzky–Golay smoothing filter.

Table 1

Bulk physical properties of the first-year ice (FYI) and second-year ice (SYI), given as mean \pm standard deviation.

	Density (kg m^{-3})	Salinity	Temperature ($^{\circ}\text{C}$)	Brine fraction (%)	Gas fraction (%)	Borehole strength (MPa)	Ice thickness (m)
FYI	911 ± 5	5.9 ± 0.3	-2.8	10.5 ± 0.5	2.8 ± 0.5	26 ± 4	0.31 ± 0.01
SYI	904 ± 5	3.1 ± 0.5	-4.0	5.5 ± 0.9	2.5 ± 0.5	41 ± 12	1.09 ± 0.10

in gas volume, with higher FYI density due to a two times higher FYI brine fraction. While the mean gas fraction was 2.5–2.8 % for both FYI and SYI, their mean brine fraction was 11 % and 5 %, respectively. FYI and SYI bulk density was $911 \pm 5 \text{ kg m}^{-3}$ and $904 \pm 5 \text{ kg m}^{-3}$, respectively, where the values are given as mean \pm standard deviation. Our FYI mean density estimates are similar to Alexandrov et al. (2010) (917 kg m^{-3}) and lower than from Jutila et al. (2022) (925 kg m^{-3}), but with significantly smaller uncertainty. Jutila et al. collected data much later during the freezing season when FYI is substantially thicker, while SYI density agrees well. The main source of this difference may be related to the high FYI gas fraction of 2.8 ± 0.5 % (assuming connected gas and brine pockets) measured during GoNorth, while typical winter values of FYI gas fraction during, for example, MOSAiC were around 1.7 %. This may be related to the relatively high bulk FYI temperature of -2.8 $^{\circ}\text{C}$ before gas bubble volume would decrease until typical winter values following Crabeck et al. (2019). Our FYI density of 911 kg m^{-3} measured on 24 October was continuing the increasing trend with FYI density of 902 kg m^{-3} in mid-September (Sinha, 1984) and $907 \pm 2 \text{ kg m}^{-3}$ in mid-October (Forsström et al., 2011). A similar increasing trend of FYI density from 893 kg m^{-3} to $908 \pm 8 \text{ kg m}^{-3}$ was observed in November at Amundsen Basin (Salganik et al., 2024).

Estimates of sea-ice density based on measurements of snow, ice thickness, and freeboard were successfully used for large-scale aerial campaigns (Jutila et al., 2022), but are characterized by large standard deviations of $15\text{--}30 \text{ kg m}^{-3}$ and higher values than from other methods. For our draft and freeboard measurements, the corresponding sea-ice density estimate was $937 \pm 23 \text{ kg m}^{-3}$ and $921 \pm 28 \text{ kg m}^{-3}$ for FYI and SYI, which indicates a 5–6 times higher spread of density values in comparison to its direct measurements. Here we used the seawater density of 1027 kg m^{-3} estimated from the measured sea-ice bottom temperature of between -1.8 $^{\circ}\text{C}$ and -1.9 $^{\circ}\text{C}$ and the snow density of 250 kg m^{-3} typical for fresh snow (Macfarlane et al., 2021). Generally, sea-ice freeboard has a large spatial variability, strongly affected by the distribution of snow and ice thickness within the studied ice floe (Thielke et al., 2023). This variability leads to sea-ice density estimates obtained from its freeboard and draft assuming hydrostatic balance not

converging even on scales of 100 m (Hutchings et al., 2015).

The SYI gas fraction was distributed within two distinct layers, above the waterline and below the upper impermeable layer, at a depth of 0.5–0.9 m (Fig. 5c). The gas layer at the ice bottom part was present only in two out of six analysed SYI cores. There was no significant correlation between brine and gas volumes, supporting that large gas volumes were not related to excessive brine losses. The SYI gas fraction was as large as 6.5 %, similar to values that may be observed in summer FYI. For our late autumn measurements, FYI gas fraction had a typical increase above its waterline, with a gas fraction of 4–10 %. Four out of six SYI cores had a distinct high-salinity layer with salinity values of 4–6 typical for FYI. These layers were located below the waterline, below 0.2–0.4 m, and above 0.8 m SYI thickness. There was no obvious relationship between layers with high salinity and high gas fractions, despite high-salinity layers having brine fractions above the permeability limit of 5 % (Fig. 5b).

We measured SYI bulk salinity of 2.3–3.8 with a mean value of 3.1 ± 0.5 , which was substantially higher than SYI bulk salinity of 1.1 ± 0.3 for MOSAiC in autumn (Fig. 5a). GoNorth SYI thickness of 1.1 m on October 24 was slightly larger than 0.8 m on October 28 for MOSAiC SYI coring site. The following increase in SYI bulk salinity for MOSAiC by mid-November is strongly related to the formation of new ice with high salinity below remnant low-salinity sea ice, which was observed in all SYI cores during the whole season. In contrast, SYI for GoNorth only experienced a minor desalination at 0.2 m from the surface with 0–1 salinity and at 0.2 m from the bottom with 1–4 salinity. Meanwhile, the middle part of SYI had a salinity of 2–7, suggesting a minor desalination but also high spatial variability typical for SYI (as around 20 % of sea ice is usually ponded (Webster et al., 2022), giving low surface salinity after the melt pond refreeze). For a similar ice thickness of 1.1 m, Wang et al. (2020) observed a mean salinity of 1.8 for Pacific Arctic FYI in August, prior to the end of the melt season and its transition into SYI. A similar salinity of 2.0 was observed by Doronin and Kheisin (1975) for Antarctic sea ice during the melt season. We measured FYI bulk salinity of 5.9 ± 0.3 , similar to 6.1 for MOSAiC measured on October 28, while FYI thickness of 0.31 m was also comparable to 0.42 m for MOSAiC. The

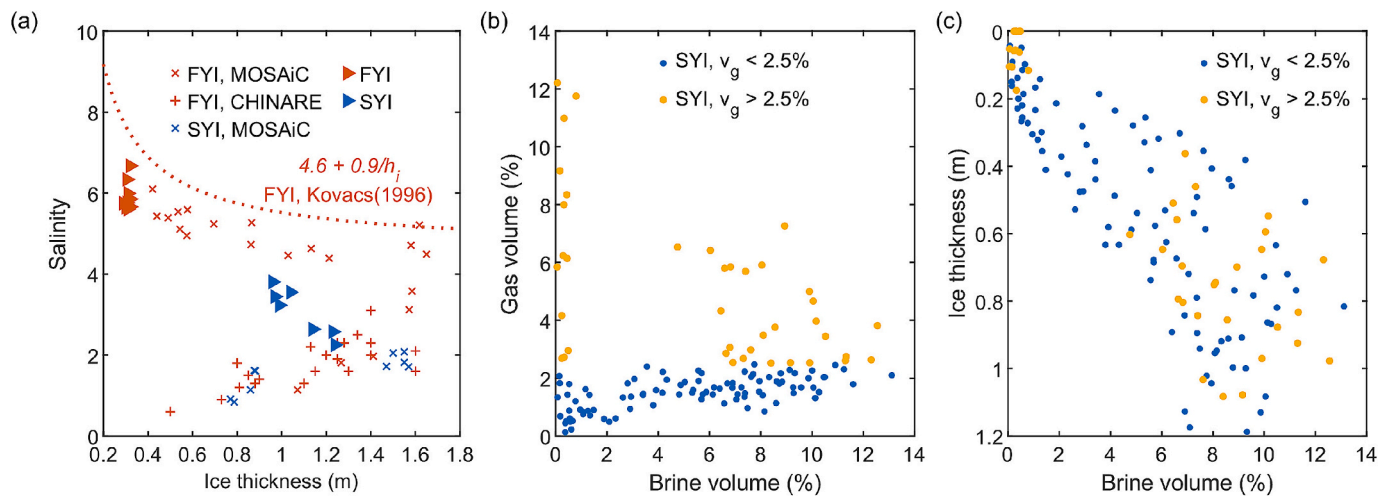


Fig. 5. Panel (a) shows the measured bulk salinity versus ice thickness for both SYI and FYI, along with MOSAic and CHINARE (Wang et al., 2020) measurements and the empirical fit from Kovacs et al. (1996) for FYI. Panel (b) shows the SYI gas fraction vs brine fraction. Panel (c) shows the vertical distribution of SYI brine fraction.

salinity of a thin FYI depends on its thickness and growth rate, as shown by Fedotov (1973). Verdugo et al. (2021) reported FYI salinity of 3.7–5.8 for 4–14 June north of Svalbard, while Peterson (2018) observed bulk salinity decrease from 6.4 to 4.8 just in 4 days in mid-June in the same location. The bulk salinity of the FYI was somewhat lower than that predicted by (Kovacs et al., 1996) for 0.31 m thick ice, illustrated in Fig. 5. This difference in salinity may be related to the thinning Arctic sea ice (Sumata et al., 2023) and corresponding slower growth rates, which lead to lower ice salinity (Griewank and Notz, 2013).

Motivated by the high salinity of SYI cores (Fig. 5a), we examined sea ice back-trajectories from the daily sea-ice drift vectors from Polar Pathfinder (Tschudi et al., 2020). The analysis of the trajectories showed that FYI stayed in Nansen Basin and drifted from the Northeast direction (83° N, 25° E; Fig. 2a). SYI drifted from Amundsen Basin further east (83° N, 129° E) in September 2021, reaching 86° N and 58° E in May 2022. Meanwhile, numerical modelling of sea-ice salinity suggested larger values of 3–4 in the region North of Franz Josef Land around 55° E (Vancoppenolle et al., 2009), which can explain similar observations of high SYI salinity during GoNorth. SYI back-trajectories in September 2022 were at 83° N, 32° E, to the Northwest from Franz Josef Land.

We estimated a SYI gas fraction of 2.2 ± 0.5 %, substantially higher than 0.9 ± 0.2 % for MOSAic, while close to winter FYI values for MOSAic of 1.7 ± 0.4 %. GoNorth FYI bulk gas fraction was 2.2 ± 0.5 % substantially lower than 3.9 % for FYI during MOSAic in summer and 3.8 % for SYI during MOSAic in early autumn. This may be explained by the transition of the GoNorth ice temperatures from typical summer to lower winter values and the corresponding decrease of gas fraction, as was shown by Crabeck et al. (2019). The bulk salinity of the FYI salinity core was identical to the salinity of nine density cores, indicating no substantial brine flushing during the hydrostatic weighing procedure.

3.2. Microstructure

There was a clear difference in the grain structure of the SYI at the indentation depth of 0.50 m below the ice surface. The core taken at grid point (10,10), co-located with the highest borehole strength, had a grain structure reminiscent of S2 ice (Fig. 6a). The grains in the columnar structure had optical axes that were randomly oriented predominantly in the horizontal direction, and very few brine and air pockets were visible. The second SYI core retrieved from grid point (10,0) contained grains that were significantly smaller in the horizontal dimension at indentation depth, reminiscent of granular ice. However, vertical sections prepared both above and below indentation depth revealed

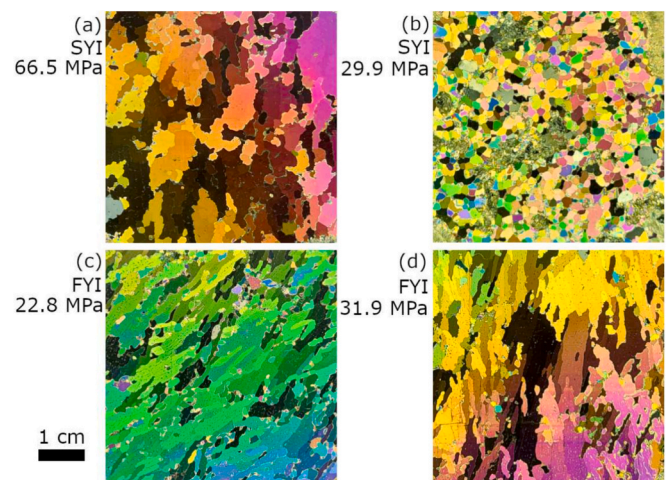


Fig. 6. Pictures of horizontal thin sections viewed in cross-polarized light, and the associated borehole strengths. For the SYI, panel (a) is from grid point (10,10) and panel (b) is from grid point (10,0), both at 0.49 m from the ice surface. For the FYI, panel (c) is from grid point (0,0) and panel (d) is from grid point (10,10), both at 0.16 m from the ice surface.

columnar structures, and it is likely that a thin granular layer was captured in the horizontal section. The grain structure of old ice can consist of a mixture of granular and columnar ice, and thin granular layers were also found by Cox et al. (1984) in multi-year ice. There were large (on the order of 1 cm) pockets visible in both horizontal and vertical sections, coinciding with the larger estimated microporosity compared to the ice at grid point (10,10).

The FYI had a granular top layer, and a transition to the start of a columnar grain structure at 0.08–0.10 m below the ice surface. In the columnar structure, the optical axes in the grains exhibited a random, preferred horizontal orientation, typical of S2 ice (Michel and Ramseier, 1971). The grain structure of both FYI cores were similar at indentation depth, 0.16 m below the ice surface. However, some grain elongation along an axis can be observed, particularly in Fig. 6c.

3.3. Mechanical measurements

A variety of failure behaviours were recorded during the borehole indentation measurements (Fig. 7). For all tests, a rapid initial pressure

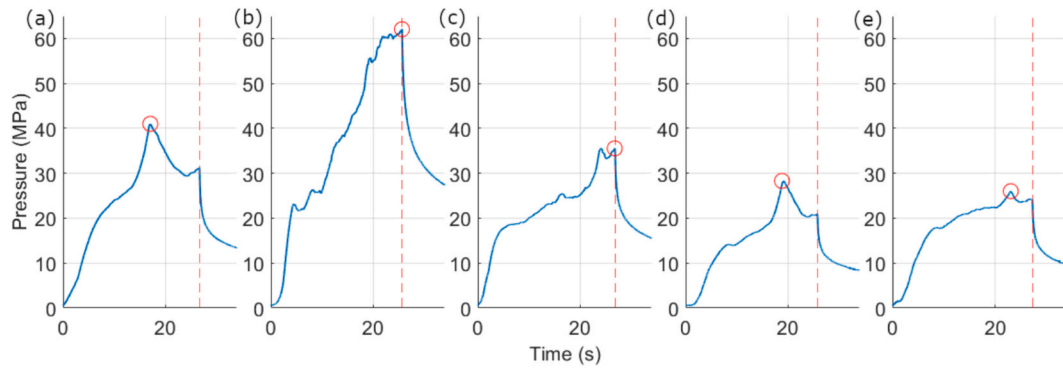


Fig. 7. Examples of typical pressure-time curves recorded during borehole indentation measurements. The highest pressure per test is marked by a red circle. The stapled vertical line marks the time where the indentation was stopped. SYI tests are shown in panels a (local coordinates (0,0)), b (10,10), and c (10,15). FYI tests are shown in panels d (10,5) and e (0,5). (For interpretation of the references to colour in this figure legend, the reader is referred to the web version of this article.)

increase in the first 5 s were seen, after which the pressure rate of increase typically started declining and the behaviours started to diverge. At the end of the tests, the indenter was stopped and left in place, and the rapid decrease after about 30 s shows the relaxation behaviour of the system (Fig. 7, stapled vertical lines). The pressure curves were generally smooth without any large, sudden decreases in pressure, seemingly indicating an absence of major fractures or spalls. However, the confined state of the indentation would prevent ice movement and thus also major load drops. For some tests, a prominent peak occurred during the indentation (Fig. 7a, d), while for other tests the highest pressure happened at the very end of the test (Fig. 7b, e). For these tests, a higher peak pressure may have occurred if the indentation had continued for longer.

Defining the borehole strength as the highest pressure recorded during the indentation, the mean borehole strengths and standard deviations were 41.0 ± 12.1 MPa for the SYI and 26.0 ± 4.4 MPa for the FYI. The larger spatial variability of the SYI borehole strength can be seen in Fig. 8. A clear outlier in terms of borehole strength can be observed at the (10,10) grid coordinate, with a borehole strength of 66.5 MPa. This grid point was observed to have substantial surface roughness and was likely more deformed. Note also the weaker borehole strengths at points (5,15) and (10,15) where the indentation was more shallow, although there was no large difference to the (5,0) and (10,0) grid points. From Fig. 8, the strongest ice, which is the thickest and least porous ice at indentation depth, seems grouped around an area running

from grid point (0,5) to (10,10). Both the FYI and the SYI were relatively warm at the depth where the indentation took place, at an estimated -3.2 °C for the SYI and -2.5 °C for the FYI.

The measured borehole strengths can be compared to the measurements summarized by Johnston (2017). They found evidence of significant changes in borehole strength throughout the year, like a large decrease in FYI strength throughout the spring and summer months, likely driven by an increase in temperature along with brine volume. However, a numerical comparison to our FYI borehole strengths is not straightforward, as the authors did not carry out measurements on FYI during the autumn months, but they did measure SYI and young multiyear ice in early October. Generally, we measured significantly higher borehole strength than those found by Johnston (2017). For FYI, they estimated a depth-averaged strength of 32 MPa at most throughout the year, compared to our 26.0 ± 4.4 MPa. However, their estimation was for significantly colder ice than ours (depth-averaged temperature of -18.4 °C), while they measured strengths closer to 10 MPa with a similar depth-averaged temperature as our FYI (-3.3 °C). For SYI, they measured depth-averaged strengths in the range of 3 MPa to 15 MPa, and individual measurements up to about 35 MPa, but still significantly lower than our measured strength of 41.0 ± 12.1 MPa. Shkhinek et al. (2010) found a pressure of 20 MPa to 25 MPa during their measurement campaigns, at an indentation rate of 4.2 mm s^{-1} .

Several precautions should be taken when comparing the borehole strengths resulting from the NTNU borehole jack used in this work and

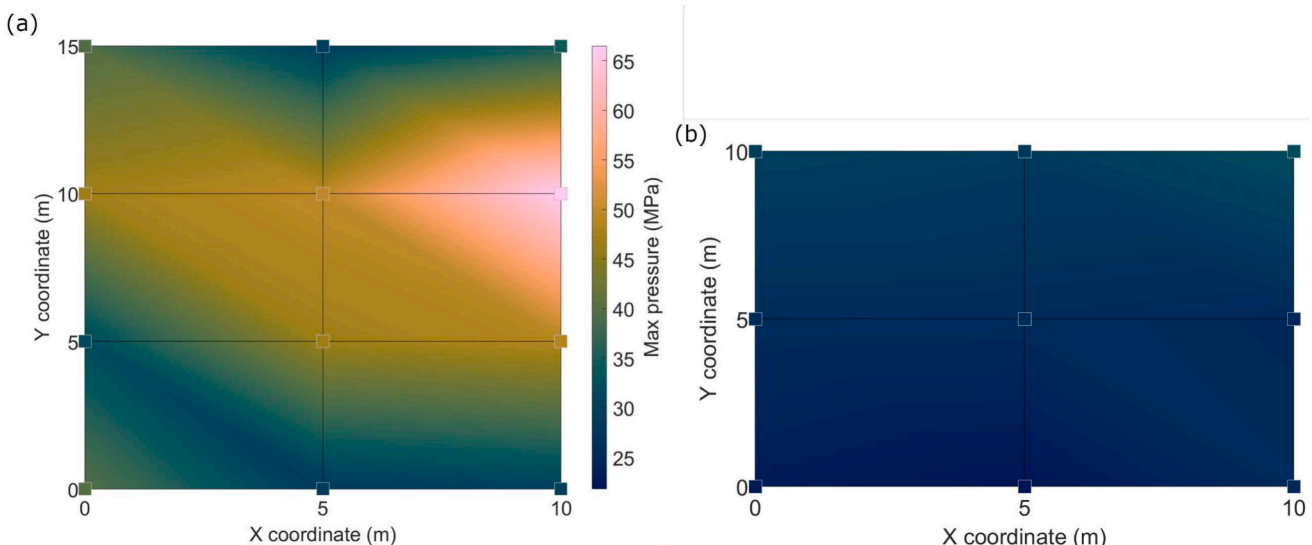


Fig. 8. Spatial distribution of mean borehole strengths for the SYI (a) and FYI (b), illustrated on the grid coordinates used for core sampling.

borehole strengths from hydraulically driven borehole jacks. The contact area of the indenter used in the NTNU BHJ ($7 \cdot 10^{-4} \text{ m}^2$) is about nine times smaller than the contact area in the most commonly used borehole jacks ($6.5 \cdot 10^{-3} \text{ m}^2$ (Sinha, 2011)), which should result in higher pressures from the indentation size effect (Kim and Schulson, 2015). In comparison to hydraulic systems, the NTNU BHJ is effectively more stiff, which by itself is expected to increase the measured strength (Sinha, 1981).

3.4. Physical properties and borehole strength

To help explain the variability in the ice borehole strength, it can be put into context with the measured physical properties of the ice at each grid location. In particular, the physical properties of the ice that is closest to the indenter are likely to affect the strength measurement. At indentation depth, the microporosity was found based on a linear interpolation of the physical properties of the four core sections closest in the vertical direction. This resulted in microporosities at an indentation depth of $7.6 \pm 3.2 \%$ for the SYI and $10.2 \pm 0.9 \%$ for the FYI. There are indications that the SYI borehole strength has a negative trend against both brine volume and microporosity at the relevant indentation depth (Fig. 9). The trend seems less clear for gas volume, although the strongest areas in the SYI contained little gas. Note that the brine volume is the greater contributor to the microporosity; thus, any trends in the strength with different microporosity will be determined mostly by the effect of the brine. For FYI, any trends in the data are less clear. The microporosity of the FYI had less variability than that of the SYI, and the range of values may be too small for any trend to appear over the overall noise in the mechanical measurements. In absolute terms, there seems to be little difference between SYI and FYI borehole strengths when taking microporosity into account. The SYI seems to only be slightly stronger than FYI, with similar microporosity at indentation depth, which may well be caused by the SYI being thicker. Indenting into the thicker SYI means a greater volume of ice is available to distribute the stress from the indentation before failure, and greater confinement. Indentations into the FYI will only have about 14 cm to the nearest free edge on average, which may decrease the measured strength. Additionally, the SYI was slightly colder at indentation depth (a difference of $0.7 \text{ }^\circ\text{C}$), which should give it greater borehole strength (Johnston, 2006). But even if there was no difference in confinement and temperature, SYI is still expected to have a greater borehole strength than FYI. For hydraulic

BHJs, measured BHJ strengths in FYI and SYI were compared by Johnston (2017), who found that SYI remained consistently stronger than FYI in all seasons. However, Johnston did not examine the borehole strength in SYI corrected for the possibly lower microporosity in SYI. Johnston used a depth-averaged strength, meaning that the strength of any porous layers in SYI may have been averaged out.

Simple linear regressions were carried out based on ordinary least squares to examine the relationship between local microporosity and borehole strength. Some regression models and their associated statistics are summarized in Table 2. From the regression models, there seems to be a much greater correlation between brine volume and microporosity compared to gas volume. Including the gas volume and considering the total microporosity only gives a minor improvement in goodness of fit compared to only considering the brine volume. Note that the large difference in correlation may be exacerbated by the small range of gas fraction values compared to brine fraction values. Using the total microporosity v_T as a variable and including data from both FYI and SYI, a relatively high R^2 of 0.82 was found. The model had a regression p -value of 0.00, seemingly indicating that there is a high likelihood of a real association between strength and microporosity (James et al., 2021). As R^2 is only a measure of how well a model fits existing data, and cannot be used to determine how well a model predicts new data, the predictive power of the models were instead estimated by the predicted R^2 statistic. The predicted R^2 is found by systematically removing one observation at a time, fitting a regression model to the remaining observations, and calculating the squared distance from the removed

Table 2

Statistics for linear regression models for borehole strength σ_B (in MPa) based on brine volume fraction v_b , gas volume fraction v_g , and total microporosity fraction v_T (all in %) at indentation depth.

Model	Data included	R^2	Predicted R^2	Standard error
$\sigma_B = (65.6 - 4.01v_b)$	FYI & SYI	0.78	0.65	6.07
$\sigma_B = (44.2 - 5.70v_g)$	FYI & SYI	0.10	0.00	12.23
$\sigma_B = (72.1 - 3.92v_T)$	FYI & SYI	0.82	0.71	5.40
$\sigma_B = (72.6 - 3.81v_T)$	SYI	0.80	0.52	6.96
$\sigma_B = (31.2 - 0.45v_T)$	FYI	0.02	0.00	3.43
$\sigma_B = (102.1 - 22.1v_T^{0.5})$	FYI & SYI	0.84	0.73	5.18

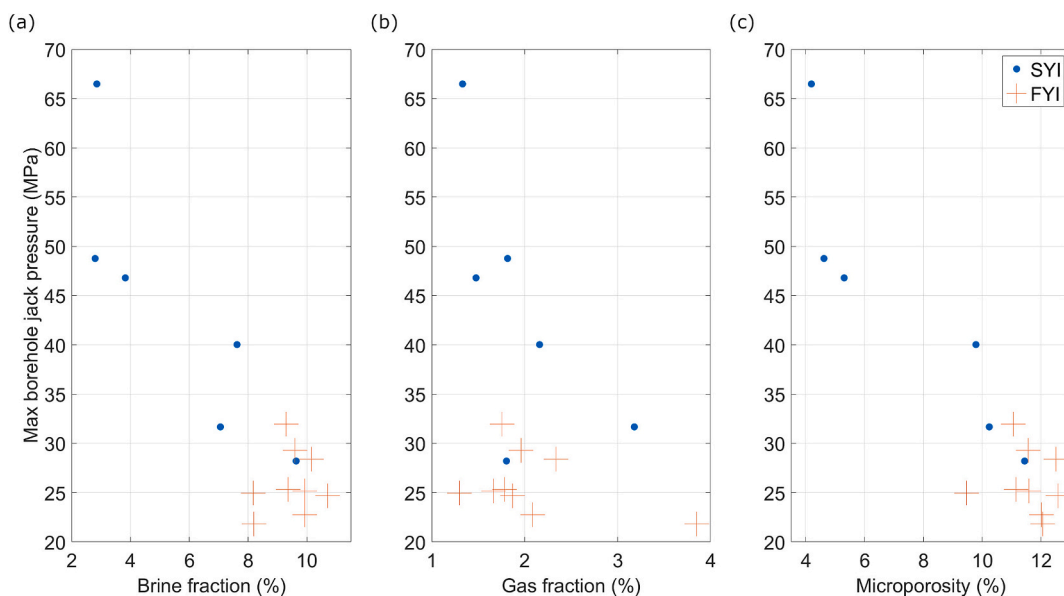


Fig. 9. Borehole strengths and brine (a), gas (b), and microporosity (c) fractions at indentation depth for SYI (blue, points) and FYI (red, plus signs). (For interpretation of the references to colour in this figure legend, the reader is referred to the web version of this article.)

observation to the fitted model (Walpole et al., 2012). The predictive power from the models, as found from the predicted R^2 statistic, was clearly lower for SYI and FYI considered separately. However, the common assumptions for linear regression were not fulfilled for any of the models, which would call the R^2 values into question. The residuals in the models were not normally distributed, and they had increasing variance with strength (i.e., exhibiting heteroskedasticity), meaning a non-linear model or a variable transformation of the borehole strength may be more appropriate (Walpole et al., 2012). Additionally, the residuals did not seem to be uncorrelated, meaning adjacent measurements were more similar than measurements further away. The correlations could originate from spatial distributions in ice strength that occurred independent of porosity, as the measurement positions were not randomized, or from trends in instrumental measurement error.

Fitting models based on the square root of the porosity or variants thereof, as suggested by Timco and Frederking (1990) and Moslet (2007) for uniaxial compressive strength, gave a slight improvement in both fit and model prediction power. The fundamental issues with the residuals were still present in these models. In the end, the problems with the residuals and the limited amount of data weaken the conclusions one might draw on the relation between microporosity and strength in this study. Note that averaging local physical properties in a greater area around the indenter depth before carrying out the regression might give a more physically plausible functional dependence, as the indenter applies stress in an area around it. However, mathematically speaking, an averaging process should also result in a greater R^2 as variability is evened out and information is lost, and it is difficult to separate the relative contribution from each of these processes from the greater R^2 for each model.

3.4.1. Spatial variability

The spatial variability across the ice sheet can be quantified through the coefficient of variation k_v :

$$k_v = \frac{\sigma}{\mu}, \quad (1)$$

where σ is the standard deviation and μ is the mean of a property. The borehole strength in SYI had appreciable spatial variability compared to FYI ($k_v = 0.29$ for SYI compared to 0.17 for FYI). This can be compared to the spatial variability of the relevant physical properties, such as the microporosity at indentation depth ($k_v = 0.43$ for SYI, 0.09 for FYI) and bulk microporosity ($k_v = 0.11$ for SYI, 0.05 for FYI). That is, the microporosity at indentation depth has greater spatial variability for SYI compared to the borehole strength, while the opposite is true for FYI.

For the SYI, it is reasonable to expect a smaller variability in strength compared to physical properties when the variability in physical properties is relatively large. Borehole indentation loads a volume of ice that is larger than the size of the indenter, meaning the bulk properties of the surrounding ice will affect the borehole strength. Variability in the physical properties of the ice over a smaller scale than the loaded ice volume will not completely translate to variability in borehole strength. Barrault and Strub-Klein (2009) used a hydraulic borehole jack with a 90 mm diameter, and found significant influence from the indentation on the surrounding ice, with 98 % of the stress concentrated in the closest 0.6 m from the borehole in the horizontal direction. Even though the NTNU borehole jack has a smaller indenter, it is reasonable to expect that the indentation loads the surrounding ice in a similar manner, though the size of the effect is unknown. Kallelid et al. (2019) used the NTNU borehole jack and found that the air bubbles in glacier ice were compressed in an area a few centimetres away from the indenter, similar to Hot Isostatic Pressing discussed in the context of ice by Sinha (2011). However, the loaded ice volume should be larger than the area where air bubbles are compressed. For the FYI, the smaller variability in the borehole strength compared to the physical properties could be

explained by a baseline measurement error in the strength measurements. An instrumental error in the borehole jack, which may be larger relative to the minor variability in physical properties, could be dominating compared to the spatial variability in the borehole strength.

A notable difference between the estimated microporosity at indentation depth for FYI and SYI is the two distinct groups of SYI microporosities in Fig. 9. From the brine volume profiles in Fig. 4, the SYI cores can roughly be divided into two groups based on the salinity layer and brine volume at indentation depth, which would result in a different microporosity. These two groups of SYI are also separated spatially, where the area with the strongest ice in Fig. 8 also has the least porous ice at indentation depth. It seems clear that there are different regimes in the ice captured by both the strength measurements and porosity estimations, possibly pointing to different thermodynamic or deformation processes occurring during summer melt. In this case, these processes resulted in significant local variability in physical properties and ice strength on the scale of 5 m to 10 m.

The spatial variability in borehole strength can be compared to studies on the variability of uniaxial compressive strength. Note that the ice experiences significantly less confinement during uniaxial compression than during borehole indentation, which may affect its inelastic behaviour and the strength comparison. However, due to the lack of previous research on spatial variability of borehole strength, the comparison to uniaxial compressive strength can still be instructive. For example, Strub-Klein and Høyland (2012) carried out uniaxial compression tests on landfast sea ice in the Van Mijenfjord on Svalbard from March to May. They generally found a higher coefficient of variation for their populations of uniaxial compression than for our borehole strength values. The only exception is their measurements in early March, which had a comparable coefficient of variation to our work (k_v of about 0.15 to 0.20). Their larger k_v may be caused by an uneven deterioration of their ice cover, which would become a notable factor compared to the freeze-up season in late autumn when we carried out our measurements. The comparison to our borehole strength variability may further be affected by a difference in failure modes. Premature or brittle failures occurring during uniaxial compression could complicate the comparison to borehole strength variability, as catastrophic premature failures were absent during our borehole indentation measurements. In this case, Strub-Klein and Høyland observed mainly ductile failure modes, though also some brittle and transitional modes. However, there was no clear correlation between the coefficients of variation and the recorded failure modes for their uniaxial compression measurements.

4. Conclusions

This study presents local measurements of the physical properties and strength of first-year ice (FYI) and second-year ice (SYI) encountered in late October 2022 in the area north of Svalbard during the GoNorth 2022 expedition. One measurement station each on FYI and SYI was carried out, resulting in 21 cores used to characterize the physical properties and microstructure of the ice. High-resolution vertical profiles of the physical properties of the ice were captured, including temperature, salinity, density, and estimated microporosity. Density measurements using hydrostatic weighing resulted in bulk densities of $911 \pm 5 \text{ kg m}^{-3}$ for FYI and $904 \pm 5 \text{ kg m}^{-3}$ for SYI.

There was a qualitative difference in the SYI seen in the measurement of thickness, physical properties, and strength, likely caused by summer processes of deformation or melt. We observed a high spatial variability of SYI gas volume, with a third of ice cores having a distinct layer with high gas volume up to 7 % at the bottom half of ice, with a corresponding low density of 860–880 kg m^{-3} . Similarly, we observed a high spatial variability of SYI salinity below its upper 0.4 m. The practical salinity of separate 5 cm long SYI sections ranged from 1 to 7 at the middle part and from 2 to 5 at the bottom part. It resulted in high variability in brine volume, which presumably led to more variable ice

confined strength.

Ice strength measurements were carried out on both SYI and FYI with the use of the NTNU borehole jack with a 3 cm wide cylindrical indenter. The borehole strength was 41.0 ± 12.1 MPa for the SYI and 26.0 ± 4.4 MPa for the FYI. For the first time, borehole strength was related to total microporosity, including gas fraction, as found from hydrostatic density measurements. The borehole strength showed indications of decreasing with microporosity at indentation depth, with brine volume being the most important contributor. However, the limited data and correlated measurements prevented us from establishing a statistical model of the relation with sufficient certainty. The greater spatial variability in the physical properties of the SYI was reflected in the borehole strength variability. The SYI was on average stronger than the FYI, although only slightly if correcting for the microporosity at indentation depth.

CRedit authorship contribution statement

Vegard Hornnes: Writing – review & editing, Writing – original draft, Visualization, Methodology, Investigation, Formal analysis, Data curation, Conceptualization. **Evgenii Salganik:** Writing – review & editing, Writing – original draft, Visualization, Methodology, Investigation, Formal analysis, Data curation, Conceptualization. **Knut Vilhelm Høyland:** Writing – review & editing, Writing – original draft, Supervision, Project administration, Funding acquisition, Conceptualization.

Declaration of competing interest

The authors declare the following financial interests/personal relationships which may be considered as potential competing interests:

Vegard Hornnes reports financial support was provided by Research Council of Norway. Evgenii Salganik reports financial support was provided by Research Council of Norway. Knut Vilhelm Høyland reports financial support was provided by Research Council of Norway. Vegard Hornnes reports a relationship with Equinor ASA that includes: employment. Evgenii Salganik reports a relationship with Norwegian Polar Institute that includes: employment. If there are other authors, they declare that they have no known competing financial interests or personal relationships that could have appeared to influence the work reported in this paper.

Data availability

All the datasets used in this study are publicly available. We strongly advise that future studies using the data presented here also cite the respective original datasets listed below. GoNorth sea-ice salinity, temperature, and density are available in [Salganik et al. \(2023a\)](#). GoNorth borehole strength data is available in [Hornnes et al. \(2024\)](#). MOSAiC ice salinity, temperature, and density are available in [Oggier et al. \(2023a\)](#) and [Oggier et al. \(2023b\)](#).

Acknowledgements

We thank all persons involved in the expedition of the Research Vessel *Kronprins Haakon* during the 2022 GoNorth expedition. We especially thank Paul Jorrit Rübsamen-Von Döhren and Nabil Panchi for their help with collecting field measurements. VH and KVH were supported by Research Council of Norway project RareIce (grant no 326834). ES was supported by Research Council of Norway project INTERAAC (grant no 328957) and HAVOC (grant no 280292).

References

Alexandrov, V., Sandven, S., Wahlin, J., Johannessen, O.M., 2010. The relation between sea ice thickness and freeboard in the arctic. *Cryosphere* 4 (3), 373–380.
 Årthun, M., Eldevik, T., Smedsrud, L.H., 2019. The role of Atlantic heat transport in future arctic winter sea ice loss. *J. Clim.* 32 (11), 3327–3341.

Barrault, S., Strub-Klein, L., 2009. An experimental set-up for measuring stress propagation in sea ice. In: *Proceedings of the International Conference on Port and Ocean Engineering Under Arctic Conditions*.

Cox, G.F.N., Weeks, W.F., 1983. Equations for determining the gas and brine volumes in sea-ice samples. *J. Glaciol.* 29 (102), 306–316.

Cox, G.F.N., Richter-Menge, J.A., Weeks, W.F., Mellor, M., Bosworth, H., 1984. *Mechanical Properties of Multi-Year Sea Ice: Phase I, Test Results*, vol. 84–9. US Army Corps of Engineers, Cold Regions Research & Engineering Laboratory.

Crabeck, O., Delille, B., Rysgaard, S., Thomas, D.N., Geilfus, N.-X., Else, B., Tison, J.-L., 2014. First “in situ” determination of gas transport coefficients (d_{O_2} , d_{Ar} and d_{N_2}) from bulk gas concentration measurements (O_2 , N_2 , Ar) in natural sea ice. *J. Geophys. Res. Oceans* 119 (10), 6655–6668.

Crabeck, O., Galley, R., Delille, B., Else, B., Geilfus, N.-X., Lemes, M., Des Roches, M., Francus, P., Tison, J.-L., Rysgaard, S., 2016. Imaging air volume fraction in sea ice using non-destructive x-ray tomography. *Cryosphere* 10 (3), 1125–1145.

Crabeck, O., Galley, R.J., Mercury, L., Delille, B., Tison, J.-L., Rysgaard, S., 2019. Evidence of freezing pressure in sea ice discrete brine inclusions and its impact on aqueous-gaseous equilibrium. *J. Geophys. Res. Oceans* 124 (3), 1660–1678.

Cramer, F., Shephard, G.E., Heron, P.J., 2020. The misuse of colour in science communication. *Nat. Commun.* 11 (1).

Dawson, G., Landy, J., Tsamados, M., Komarov, A.S., Howell, S., Heorton, H., Krumpfen, T., 2022. A 10-year record of arctic summer sea ice freeboard from cryosat-2. *Remote Sens. Environ.* 268, 112744.

Doronin, Y., Kheisin, D., 1975. *Sea Ice, 1977*. Oxonian Press Pvt. Ltd., Y.U. Kathavate and V.S. Kothekar, Translators.

Eicken, H., 1994. Structure of under-ice melt ponds in the central arctic and their effect on the sea-ice cover. *Limnol. Oceanogr.* 39 (3), 682–693.

Fedotov, V., 1973. Studies of antarctic fast ice. In: *Iakovlev, G. (Ed.), Studies in Ice Physics and Ice Engineering*, vol. 300. Arctic and Antarctic Scientific Research Institute, pp. 95–111.

Fons, S., Kurtz, N., Bagnardi, M., 2023. A decade-plus of antarctic sea ice thickness and volume estimates from cryosat-2 using a physical model and waveform fitting. *Cryosphere* 17 (6), 2487–2508.

Forsström, S., Gerland, S., Pedersen, C.A., 2011. Thickness and density of snow-covered sea ice and hydrostatic equilibrium assumption from in situ measurements in fram strait, the barents sea and the svalbard coast. *Ann. Glaciol.* 52 (57), 261–270.

Frankenstein, G., Garner, R., 1967. Equations for determining the brine volume of sea ice from -0.5° to -22.9° C. *J. Glaciol.* 6 (48), 943–944.

Griewank, P.J., Notz, D., 2013. Insights into brine dynamics and sea ice desalination from a 1-d model study of gravity drainage. *J. Geophys. Res. Oceans* 118 (7), 3370–3386.

Hendrikse, H., Nord, T.S., 2019. Dynamic response of an offshore structure interacting with an ice floe failing in crushing. *Mar. Struct.* 65, 271–290.

Hornnes, V., Salganik, E., Döhren, P.J.R.-V., Panchi, N., Høyland, K.V., 2024. Borehole Indentation Strength of First- and Second-Year Sea-Ice during Gonorth 2022 Leg 1.

Hutchings, J.K., Heil, P., Lecomte, O., Stevens, R., Steer, A., Lieser, J.L., 2015. Comparing methods of measuring sea-ice density in the east antarctic. *Ann. Glaciol.* 56 (69), 77–82.

ISO 19906, 2019. ISO 19906:2019(en) Petroleum and Natural Gas Industries – Arctic Offshore Structures. International Organization for Standardization, Geneva, Switzerland.

James, G., Witten, D., Hastie, T., Tibshirani, R., 2021. *An Introduction to Statistical Learning*, 2nd edition. Springer Science+Business Media.

Johnston, M., 2006. A comparison of physical properties and strength of decaying first-year ice in the arctic and sub-arctic. *Ann. Glaciol.* 44, 154–162.

Johnston, M., 2014. A decade of probing the depths of thick multi-year ice to measure its borehole strength. *Cold Reg. Sci. Technol.* 99, 46–65.

Johnston, M., 2017. Seasonal changes in the properties of first-year, second-year and multi-year ice. *Cold Reg. Sci. Technol.* 141, 36–53.

Jutila, A., Hendricks, S., Ricker, R., von Albedyll, L., Krumpfen, T., Haas, C., 2022. Retrieval and parameterisation of sea-ice bulk density from airborne multi-sensor measurements. *Cryosphere* 16 (1), 259–275.

Kallelid, M.S., 2018. A Study of the Strength and the Physical Properties of Glacier-Ice Runways-Assesment of Troll Airfield, Antarctica. Master’s thesis. NTNU.

Kallelid, M.S., Nord, T.S., Lidström, S., 2019. The strength and the physical properties of glacier-ice runways. In: *Proceedings of the International Conference on Port and Ocean Engineering Under Arctic Conditions*.

Kern, S., Khvorostovsky, K., Skourup, H., Rinne, E., Parsakhoo, Z., Djepa, V., Wadhams, P., Sandven, S., 2015. The impact of snow depth, snow density and ice density on sea ice thickness retrieval from satellite radar altimetry: results from the esa-cci sea ice cvc project round robin exercise. *Cryosphere* 9 (1), 37–52.

Kim, E., Schulson, E.M., 2015. A phenomenological explanation of the pressure-area relationship for the indentation of ice: two size effects in spherical indentation experiments. *Cold Reg. Sci. Technol.* 115, 48–55.

Koenig, Z., Provost, C., Sennéchal, N., Garric, G., Gascard, J.-C., 2017. The yermak pass branch: a major pathway for the Atlantic water north of svalbard? *J. Geophys. Res. Oceans* 122 (12), 9332–9349.

Kovacs, A., 1997. Estimating the full-scale flexural and compressive strength of first-year sea ice. *J. Geophys. Res. Oceans* 102 (C4), 8681–8689.

Kovacs, A., RESEARCH, C. R. NH., E. L. H., of Engineers, U. S. A. C., Research, C. R. (U.S.), E. L., 1996. *Sea Ice: Bulk Salinity Versus Ice Floe Thickness*. Number pt. 1 in CRREL report. U.S. Army Cold Regions Research and Engineering Laboratory.

Landy, J.C., Petty, A.A., Tsamados, M., Stroeve, J.C., 2020. Sea ice roughness overlooked as a key source of uncertainty in cryosat-2 ice freeboard retrievals. *J. Geophys. Res. Oceans* 125 (5).

- Landy, J.C., Dawson, G.J., Tsamados, M., Bushuk, M., Stroeve, J.C., Howell, S.E.L., Krumpen, T., Babb, D.G., Komarov, A.S., Heorton, H.D.B.S., Belter, H.J., Aksenov, Y., 2022. A year-round satellite sea-ice thickness record from CryoSat-2. *Nature* 609 (7927), 517–522.
- Langway, C., 1958. Ice fabrics and the universal stage. In: Technical Report 62 U.S. Army Corps of Engineers, Snow, Ice and Permafrost Research Establishment.
- Leppäranta, M., Manninen, T., 1988. The Brine and Gas Content of Sea Ice with Attention to Low Salinities and High Temperatures.
- Liu, Z., Risi, C., Codron, F., Jian, Z., Wei, Z., He, X., Poulsen, C.J., Wang, Y., Chen, D., Ma, W., Cheng, Y., Bowen, G.J., 2022. Atmospheric forcing dominates winter barents-Kara Sea ice variability on interannual to decadal time scales. *Proc. Natl. Acad. Sci.* 119 (36).
- Lundesgaard, O., Sundfjord, A., Lind, S., Nilsen, F., Renner, A.H.H., 2022. Import of Atlantic water and sea ice controls the ocean environment in the northern barents sea. *Ocean Sci.* 18 (5), 1389–1418.
- Macfarlane, A.R., Schneebeli, M., Dadic, R., Wagner, D.N., Arndt, S., Clemens-Sewall, D., Hämmerle, S., Hannula, H.-R., Jaggi, M., Kolabutin, N., Krampe, D., Lehning, M., Matero, I., Nicolaus, M., Oggier, M., Pirazzini, R., Polashenski, C., Raphael, I., Regnery, J., Shimanuchuk, E., Smith, M.M., Tavri, A., 2021. Snowpit Raw Data Collected during the MOSAiC Expedition.
- Michel, B., Ramseier, R., 1971. Classification of river and lake ice. *Can. Geotech. J.* 8 (1), 36–45.
- Moreau, S., Vancoppenolle, M., Zhou, J., Tison, J.-L., Delille, B., Goosse, H., 2014. Modelling argon dynamics in first-year sea ice. *Ocean Model.* 73, 1–18.
- Moslet, P.O., 2007. Field testing of uniaxial compression strength of columnar sea ice. *Cold Reg. Sci. Technol.* 48 (1), 1–14.
- Nakawo, M., 1983. Measurements on air porosity of sea ice. *Ann. Glaciol.* 4, 204–208. National Geophysical Data Center, 2006. Etopo2v2 2-minute Global Relief Model.
- Notz, D., Worster, M.G., 2008. In situ measurements of the evolution of young sea ice. *J. Geophys. Res. Oceans* 113 (C3).
- Oggier, M., Salganik, E., Whitmore, L., Fong, A.A., Hoppe, C.J.M., Rember, R., Høyland, K.V., Divine, D.V., Gradinger, R., Fons, S.W., Abrahamsson, K., Aguilar-Islas, A.M., Angelopoulos, M., Arndt, S., Balmonte, J.P., Bozzato, D., Bowman, J.S., Castellani, G., Chamberlain, E., Creamean, J., D'Angelo, A., Damm, E., Dumitrascu, A., Eggers, S.L., Gardner, J., Grosfeld, L., Haapala, J., Immerz, A., Kolabutin, N., Lange, B.A., Lei, R., Marsay, C.M., Maus, S., Müller, O., Olsen, L.M., Nuibom, A., Ren, J., Rinke, A., Sheikin, I., Shimanuchuk, E., Snoeijs-Leijonmalm, P., Spahic, S., Stefels, J., Torres-Valdés, S., Torstensson, A., Ulfso, A., Verdugo, J., Vortkamp, M., Wang, L., Webster, M., Wischniewski, L., Granskog, M.A., 2023a. First-Year Sea-Ice Salinity, Temperature, Density, Oxygen and Hydrogen Isotope Composition from the Main Coring Site (Mcs-Fyi) during Mosaic Legs 1 to 4 in 2019/2020.
- Oggier, M., Salganik, E., Whitmore, L., Fong, A.A., Hoppe, C.J.M., Rember, R., Høyland, K.V., Gradinger, R., Divine, D.V., Fons, S.W., Abrahamsson, K., Aguilar-Islas, A.M., Angelopoulos, M., Arndt, S., Balmonte, J.P., Bozzato, D., Bowman, J.S., Castellani, G., Chamberlain, E., Creamean, J., D'Angelo, A., Damm, E., Dumitrascu, A., Eggers, L., Gardner, J., Grosfeld, L., Haapala, J., Immerz, A., Kolabutin, N., Lange, B.A., Lei, R., Marsay, C.M., Maus, S., Olsen, L.M., Müller, O., Nuibom, A., Ren, J., Rinke, A., Sheikin, I., Shimanuchuk, E., Snoeijs-Leijonmalm, P., Spahic, S., Stefels, J., Torres-Valdés, S., Torstensson, A., Ulfso, A., Verdugo, J., Vortkamp, M., Wang, L., Webster, M., Wischniewski, L., Granskog, M.A., 2023b. Second-Year Sea-Ice Salinity, Temperature, Density, Oxygen and Hydrogen Isotope Composition from the Main Coring Site (Mcs-Syi) during Mosaic Legs 1 to 4 in 2019/2020.
- Perovich, D.K., Richter-Menge, J.A., Jones, K.F., Light, B., Elder, B.C., Polashenski, C., Laroche, D., Markus, T., Lindsay, R., 2011. Arctic Sea-ice melt in 2008 and the role of solar heating. *Ann. Glaciol.* 52 (57), 355–359.
- Peterson, A.K., 2018. Observations of brine plumes below melting arctic sea ice. *Ocean Sci.* 14 (1), 127–138.
- Peterson, A.K., Fer, I., McPhee, M.G., Randelhoff, A., 2017. Turbulent heat and momentum fluxes in the upper ocean under arctic sea ice. *J. Geophys. Res. Oceans* 122 (2), 1439–1456.
- Pustogvar, A., Kulyakhtin, A., 2016. Sea ice density measurements. Methods and uncertainties. *Cold Reg. Sci. Technol.* 131, 46–52.
- Ricker, R., Hendricks, S., Kaleschke, L., Tian-Kunze, X., King, J., Haas, C., 2017. A weekly arctic sea-ice thickness data record from merged CryoSat-2 and SMOS satellite data. *Cryosphere* 11 (4), 1607–1623.
- Rødtang, E., John, J., Alfredsen, K., Høyland, K., 2023. In-situ ice strength distribution of anchor ice dams. *Cold Reg. Sci. Technol.* 215, 103982.
- Salganik, E., Hornnes, V., Döhren, P.J.R.-V., Panchi, N., Høyland, K.V., 2023a. First- and Second-Year Sea-Ice Salinity, Temperature, and Density during Gonorth 2022 Leg 1.
- Salganik, E., Katlein, C., Lange, B., Matero, I., Lei, R., Fong, A., Fons, S., Divine, D., Oggier, M., Castellani, G., Bozzato, D., Chamberlain, E., Hoppe, C., Müller, O., Gardner, J., Rinke, A., Pereira, P., Ulfso, A., Marsay, C., Webster, M., Maus, S., Høyland, K., Granskog, M., 2023b. Temporal evolution of under-ice meltwater layers and false bottoms and their impact on summer arctic sea ice mass balance. *Elementa Sci. Anthropocene* 11 (1), 00035, 000089.
- Salganik, E., Lange, B.A., Katlein, C., Matero, I., Anhaus, P., Muilwijk, M., Høyland, K.V., Granskog, M.A., 2023c. Observations of preferential summer melt of arctic sea-ice ridge keels from repeated multibeam sonar surveys. *Cryosphere* 17 (11), 4873–4887.
- Salganik, E., Crabeck, O., Fuchs, N., Hutter, N., Anhaus, P., Landy, J.C., 2024. Impacts of air fraction increase on arctic sea-ice thickness retrieval during melt season. *EGU sphere[preprint]*.
- Shkhinek, K., Jilenkov, A., Smirnov, V., Thomas, G., 2010. Analysis of borehole jack records. In: 20th IAHR International Symposium on Ice.
- Shokr, M., Sinha, N.K., 2015. Sea Ice: Physics and Remote Sensing. Wiley, Hoboken, New Jersey, USA.
- Sinha, N.K., 1977. Technique for studying structure of sea ice. *J. Glaciol.* 18 (79), 315–324.
- Sinha, N.K., 1981. Rate sensitivity of compressive strength of columnar-grained ice. *Exp. Mech.* 21, 209–218.
- Sinha, N.K., 1984. Uniaxial compressive strength of first-year and multi-year sea ice. *Can. J. Civ. Eng.* 11 (1), 82–91.
- Sinha, N.K., 2011. Borehole indenter - a tool for assessing in-situ bulk ice strength and micromechanics. *Cold Reg. Sci. Technol.* 69 (1), 21–38.
- Strub-Klein, L., Høyland, K.V., 2012. Spatial and temporal distributions of level ice properties: experiments and thermo-mechanical analysis. *Cold Reg. Sci. Technol.* 71, 11–22.
- Sumata, H., de Steur, L., Divine, D.V., Granskog, M.A., Gerland, S., 2023. Regime shift in arctic ocean sea ice thickness. *Nature* 615 (7952), 443–449.
- Thielke, L., Fuchs, N., Spreen, G., Tremblay, B., Birnbaum, G., Huntemann, M., Hutter, N., Itkin, P., Jutila, A., Webster, M.A., 2023. Preconditioning of summer melt ponds from winter sea ice surface temperature. *Geophys. Res. Lett.* 50 (4).
- Timco, G., Frederking, R., 1990. Compressive strength of sea ice sheets. *Cold Reg. Sci. Technol.* 17 (3), 227–240.
- Timco, G., Frederking, R., 1996. A review of sea ice density. *Cold Reg. Sci. Technol.* 24 (1), 1–6.
- Timco, G., Weeks, W., 2010. A review of the engineering properties of sea ice. *Cold Reg. Sci. Technol.* 60 (2), 107–129.
- Tschudi, M., Meier, W.N., Stewart, J.S., Fowler, C., Maslanik, J., 2019. Polar Pathfinder Daily 25 Km Ease-Grid Sea Ice Motion Vectors, Version 4.
- Tschudi, M.A., Meier, W.N., Stewart, J.S., 2020. An enhancement to sea ice motion and age products at the national snow and ice data center (nsidc). *Cryosphere* 14 (5), 1519–1536.
- Untersteiner, N., 1968. Natural desalination and equilibrium salinity profile of perennial sea ice. *J. Geophys. Res.* (1896–1977) 73 (4), 1251–1257.
- Vancoppenolle, M., Bitz, C.M., Fichefet, T., 2007. Summer landfast sea ice desalination at point barrow, Alaska: Modeling and observations. *J. Geophys. Res. Oceans* 112 (C4).
- Vancoppenolle, M., Fichefet, T., Goosse, H., 2009. Simulating the mass balance and salinity of arctic and antarctic sea ice. 2. Importance of sea ice salinity variations. *Ocean Model.* 27 (1–2), 54–69.
- Verdugo, J., Damm, E., Nikolopoulos, A., 2021. Methane cycling within sea ice: results from drifting ice during late spring, north of svalbard. *Cryosphere* 15 (6), 2701–2717.
- Walpole, R.E., Myers, R.H., Myers, S.L., Ye, K., 2012. Probability & Statistics for Engineers & Scientists, 9th edition. Pearson.
- Wang, Q., Lu, P., Leppäranta, M., Cheng, B., Zhang, G., Li, Z., 2020. Physical properties of summer sea ice in the pacific sector of the arctic during 2008–2018. *J. Geophys. Res. Oceans* 125 (9).
- Wang, Q., Liu, Y., Lu, P., Li, Z., 2023. The porosity effect on the mechanical properties of summer sea ice in the arctic. *Cryosphere Discuss.* 2023, 1–21.
- Webster, M.A., Holland, M., Wright, N.C., Hendricks, S., Hutter, N., Itkin, P., Light, B., Linhardt, F., Perovich, D.K., Raphael, I.A., Smith, M.M., von Albedyll, L., Zhang, J., 2022. Spatiotemporal evolution of melt ponds on Arctic Sea ice: MOSAiC observations and model results. *Elementa Sci. Anthropocene* 10 (1), 000072.
- Woodgate, R.A., Aagaard, K., Muench, R.D., Gunn, J., Björk, G., Rudels, B., Roach, A., Schauer, U., 2001. The arctic ocean boundary current along the eurasian slope and the adjacent Lomonosov ridge: Water mass properties, transports and transformations from moored instruments. *Deep-Sea Res. I Oceanogr. Res. Pap.* 48 (8), 1757–1792.
- Worby, A.P., Geiger, C.A., Paget, M.J., Van Woert, M.L., Ackley, S.F., DeLiberty, T.L., 2008. Thickness distribution of antarctic sea ice. *J. Geophys. Res. Oceans* 113 (C5).